Quaternary Research

doi:10.1017/qua.2019.36

A southern and northern control on speleothem-based Asian summer monsoon variability during MIS 4

Dianbing Liu*, Shushuang Liu, Yifan Fang

School of Geography, Nanjing Normal University, Nanjing 210023, China
*Corresponding author at: School of Geography, Nanjing Normal University, Nanjing 210023, China. E-mail address: ldb9921@njnu.edu.cn (D.B. Liu).

(Received October 15, 2018; Accepted May 22, 2019)

Abstract

A 20-year-resolution speleothem $\delta^{18}O$ record from southern China reveals a detailed Asian summer monsoon (ASM) history between 73.6 and 62.3 ka. ASM changes during Interstadial 19 and late MIS 4 matched Greenland temperature variations but were antiphased with Antarctic temperatures. However, long-term strengthening of the ASM in early MIS 4 agrees well with the gradual Antarctic warming, when Greenland remained in a stable cold state. More specifically, the ASM was less variable during peak interstadials in contrast to striking instabilities during stadials. These observations suggest that the factors dominating ASM variability change through time. During early MIS 4, negligible freshwater perturbations occurred in the North Atlantic, and sea-surface temperatures in the low- to midlatitude Pacific Ocean reached the modern level. Thus, an expansion of the Intertropical Convergence Zone (ITCZ) was likely important for the long-term ASM rise. In late MIS 4, the antiphase correlation between ASM and Antarctic temperature could be attributed to freshwater inputs into the North Atlantic and a southerly positioned ITCZ. Consequently, meridional ITCZ shifts, although within a limited latitudinal band, would result in an antiphase relationship between interhemispheric climate changes. Otherwise, an in-phase correlation could be expected if the centroid of ITCZ is stable along the equator.

Keywords: Speleothem record; ASM variability; MIS 4; Interhemispheric climate correlation; Expansion/contraction of ITCZ

INTRODUCTION

Shifts of the Intertropical Convergence Zone (ITCZ), an important forcing agent for Asian summer monsoon (ASM) variability (Webster et al., 1998; Wang et al., 2014, 2017; An et al., 2015), are believed to have been highly sensitive to freshwater perturbations in the North Atlantic (Broccoli et al., 2006; Stouffer et al., 2006). In these modeling studies, the ITCZ is southerly positioned when the Northern Hemisphere cools. In response to the interhemispheric thermal gradient, the ITCZ in the Pacific Ocean was reported to shift southward across a large latitudinal band, i.e., 4° south of its modern position in Heinrich Stadial (HS) 11 (Jacobel et al., 2016), 5° during the Little Ice Age (Sachs et al., 2009), and about 2.5° to 7° in the last glaciation (Reimi and Marcantonio, 2016). However, the ITCZ movement in these studies is traced by the rainfall maximum, not by the precipitation centroid (McGee et al., 2018), hampering a full understanding of past ITCZ changes and the dynamics involved.

Constraining the ITCZ location as the median latitude of zonally averaged precipitation between 20°N and 20°S (Donohoe et al., 2013; McGee et al., 2014) suggests that the ITCZ moves within a narrow latitude range, about 1° to 2° (Donohoe et al., 2013; McGee et al., 2014, 2018). In addition, a symmetrical expansion/contraction of ITCZ along the equator, rather than a latitudinal migration, has increasingly been proposed (Collins et al., 2011; Yan et al., 2015; Denniston et al., 2016). If the expansion/contraction mode dominates, climate changes within the Northern and Southern Hemispheres would be synchronous. When a latitudinal shift happens, contrasting climate conditions (warming/cooling or greater precipitation/drought) would be expected between two hemispheres. Thus, the role of ITCZ in abrupt climate changes (Steffensen et al., 2008; Thomas et al., 2009) should be further evaluated. We present here a high-resolution speleothem-based ASM record during Marine Isotope Stage (MIS) 4 from Wulu Cave, southern China, that we have used to explore in detail ASM variability and its relationship with interhemispheric climate changes.

Cite this article: Liu, D., Liu, S., Fang, Y. 2019. A southern and northern control on speleothem-based Asian summer monsoon variability during MIS 4. *Quaternary Research* 92, 738–753. https://doi.org/10.1017/qua.2019.36

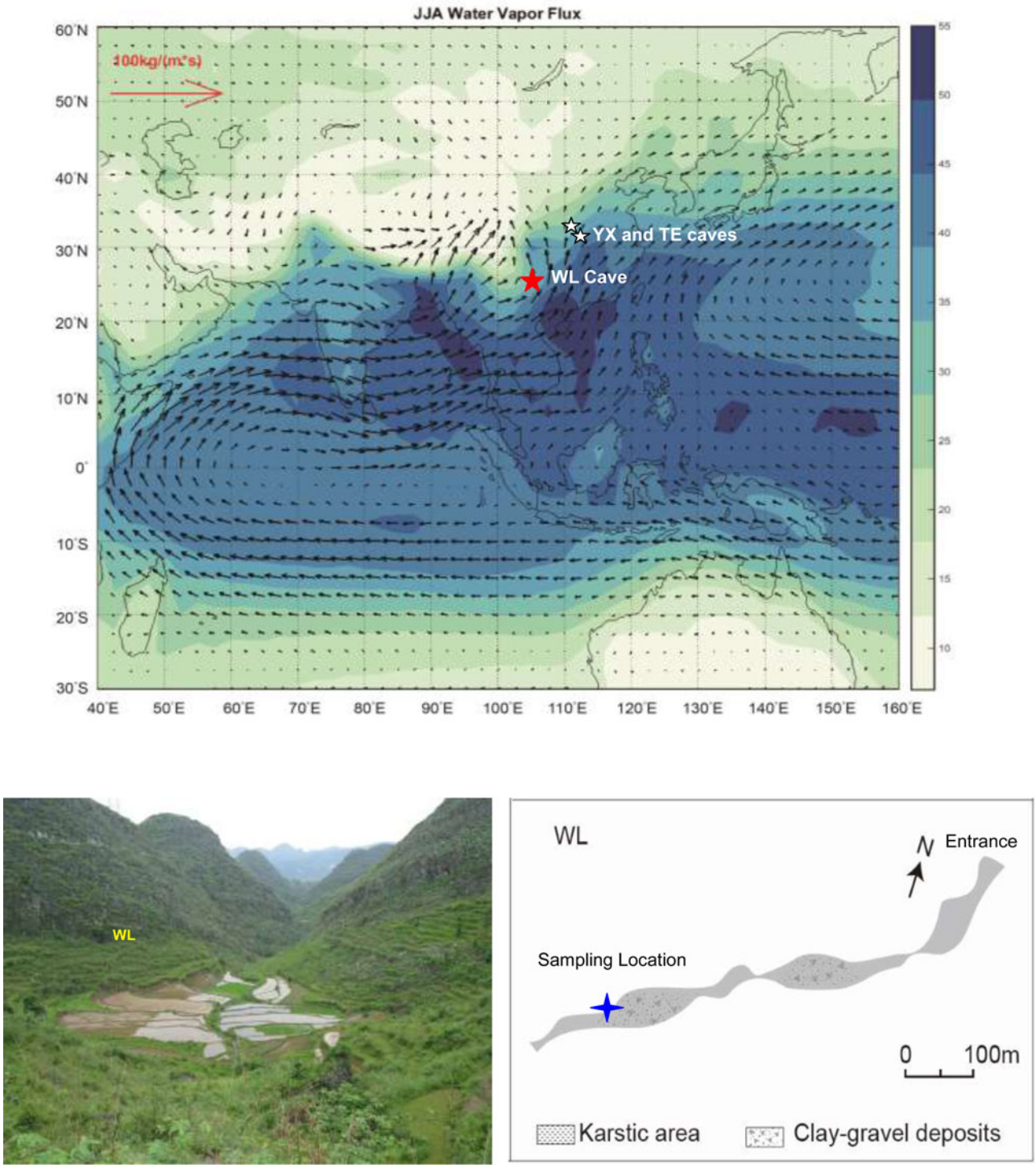

Figure 1. Study locations and the general circulation pattern of the Asian summer monsoon (ASM; June–August) between 1979 and 2016 (NCAR/NCFP, Kalnay et al., 1996). The red star represents Wulu (WL) Cave, and the white stars show Tian'e (TE; Zhang et al., 2018) and Yongxing Caves (YX; Chen et al., 2016). The arrowed lines show the average circulation field of the ASM at 700 hPa between 1979 and 2016. In the right bottom panel, the cave site and surrounding environments are indicated, with a schematic map of WL and the sampling location (blue star) shown on the left. (For interpretation of the references to color in this figure legend, the reader is referred to the web version of this article.)

CAVE SITE, SAMPLE, AND METHODS

Wulu Cave is located at the Yun-Gui Plateau in southern China (26°3′N, 105°5′E, 1440 m asl) (Fig. 1). Modern vegetation at this site is mostly composed of deciduous herbs. The cave is about 800 m long, overlain by 40 m of Triassic limestone bedrock. The regional climate conditions are

https://doi.org/10.1017/qua.2019.36 Published online by Cambridge University Press

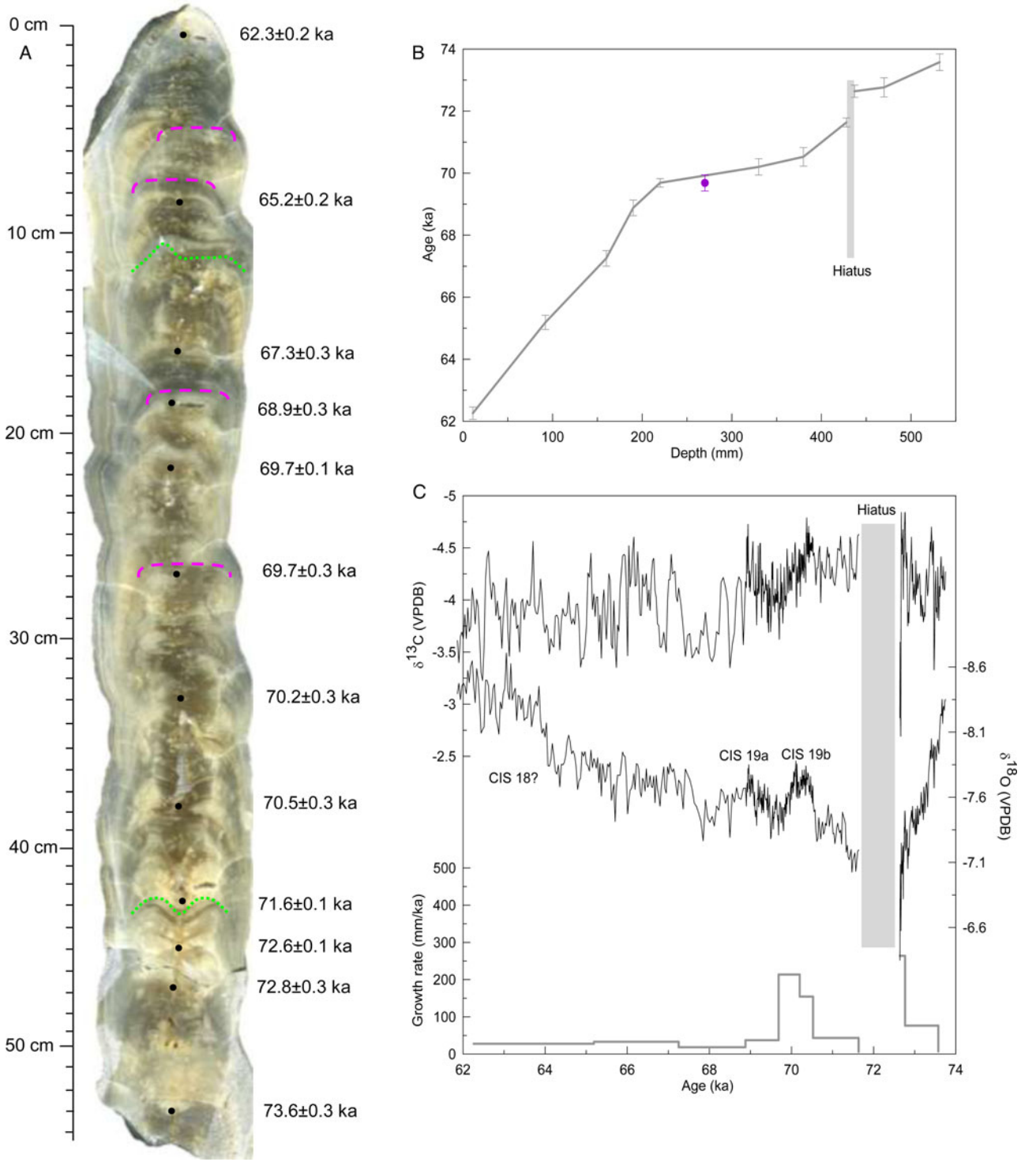

Figure 2. Slabbed section (A), age model (B), isotopic and growth rate records (C) for stalagmite Wu87. On the polished section, black dots, pink dashed lines, and green dotted lines label dating points, lithologic interfaces of dissolutional erosion, and zones of reduced growth, respectively. These surfaces were correspondingly defined as types E and L in Railsback et al. (2013). Gray bar in B and C represents the growth hiatus, and the purple dot in B indicates the rejected age. (For interpretation of the references to color in this figure legend, the reader is referred to the web version of this article.)

influenced by the subtropical East Asian and tropical Indian summer monsoons. Annual mean temperature at this site is about 14°C (1981–2015), with a maximum monthly mean value of 20.8°C in July and a minimum of 4.3°C in January. The annual mean precipitation is about 1400 mm, peaking (900 mm) during the summer (June through September), and significantly decreasing (80 mm) in the winter (December to February).

https://doi.org/10.1017/qua.2019.36 Published online by Cambridge University Press

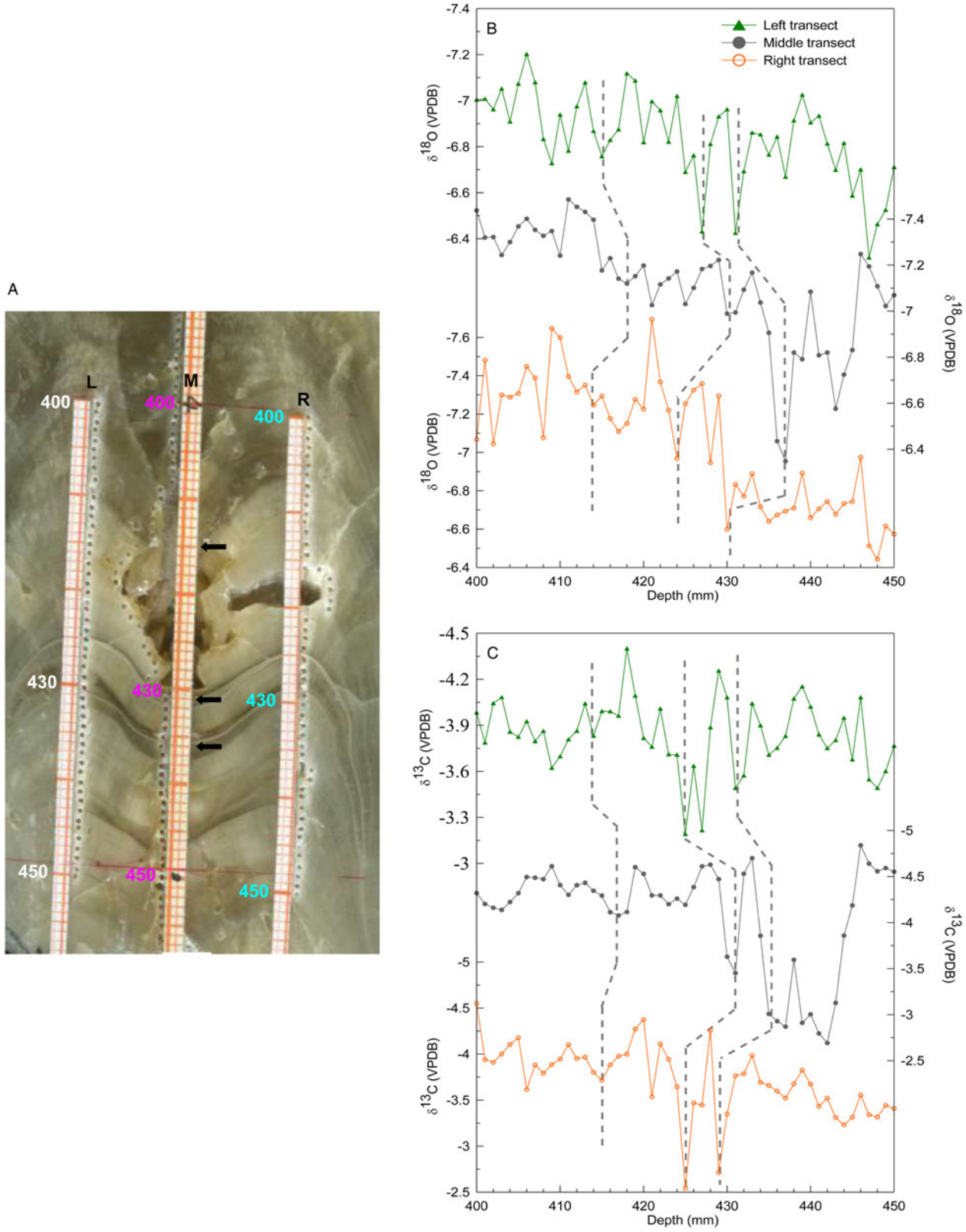

Figure 3. Evaluation on isotopic signals across the dissolutional erosion section (between 400 and 450 mm). Two additional transects were chosen for isotopic subsample collection on the polished section (A), in which "L" shows the left transect, "R" represents the right, and "M" means the middle. Numbers on the polished section show depths of subsample collection, and arrows indicate observed lithological interfaces. $\delta^{18}O$ results are indicated in B (green, left; gray, middle; orange, right), and $\delta^{13}C$ results in C. In these panels, dashed lines depict positions of arrows on the middle transect and the equivalent depths on the right and left. This shows that at least 5- to 7-mm-thick calcite had been dissolved. For comparison, the isotopic data points were not truncated according to the growth cessation (between 428 and 436 mm). (For interpretation of the references to color in this figure legend, the reader is referred to the web version of this article.)

https://doi.org/10.1017/qua.2019.36 Published online by Cambridge University Press

Stalagmite Wu87 was collected about 600 m from the cave entrance (Fig. 1). It is 545 mm high, with a candle shape, indicating a relatively stable growth history (Fig. 2A). This stalagmite is composed of translucent calcite. Along the central growth axis, dissolutional erosion of calcite occurs at about 119 and 430 mm (Fig. 2A, green dotted lines, and Fig. 3A, enlarged view). Immediately above 430 mm, large voids can be observed on the polished section, suggesting unsaturated conditions of infiltration waters across these depths. Beneath 50, 80, 172, and 267 mm, the apex of stalagmite diminishes toward the flank, indicating decreased dripwater during these periods (Fig. 2A, pink dashed lines). These lithological interfaces are similar to the type E and L layer-bounding surfaces defined by Railsback et al. (2013). As suggested by those authors, the type E surface is caused by abundant undersaturated dripwater and represents dissolutional erosion, while the type L surface is attributed to diminished dripwater and indicates reduced growth.

Twelve powder subsamples were collected along the growth axis with 0.9-mm-diameter carbide dental burrs for ^{230}Th dating. The measurements were performed on a Neptune multicollector inductively coupled plasma mass spectrometer at the School of Geography, Nanjing Normal University. The chemical procedures used to separate uranium and thorium and the age determinations are similar to those described in Shao et al. (2017). Half-life values for ^{234}U and ^{230}Th used in this study are 245,620 ± 260 and 75,584 ± 110 years, respectively (Cheng et al., 2013). Dating results are listed in Table 1, with typical analytical errors (2σ) ranging from 100 to 300 years. For stable isotopic measurements, 545 subsamples were drilled with 0.3-mm-diameter carbide dental burrs. Analyses were performed on an online automated carbonate preparation system (Kiel) linked to a Finnigan MAT-253 mass spectrometer at the School of Geography, Nanjing Normal University. Spatial resolution is 1 mm, equivalent to an average temporal resolution of 20 years, according to our age model. Standards were run every 10 to 15 samples, and duplicates were run every 15 to 20 samples to check for nonlinearity. The results are reported relative to Vienna Pee Dee Belemnite, with standardization determined relative to NBS 19 (+1.95‰ for δ^{18}O and −2.2‰ for δ^{13}C). Precision of δ^{18}O values is 0.06‰ at the 1σ level.

RESULTS

Chronology

Twelve ^{230}Th dates reveal that sample Wu87 grew during the MIS 4, spanning 73.6 ± 0.3 to 62.3 ± 0.2 ka (Table 1). The ages for isotopic data were established with linear interpolation between adjacent dates. Two dates at 428 and 437 mm (71.6 ± 0.1 ka; 72.6 ± 0.1 ka) bracketing the dissolutional interface (between 429 and 436 mm) suggest a growth cessation of about 1000 years at this depth (Fig. 2A, green dotted line). In addition, the dating result at 270 mm (69.7 ± 0.3 ka) (Fig. 2B, purple dot) is very similar to that at 220 mm (69.7 ± 0.1 ka) (Table 1), which was rejected in establishing the age–depth relationship. The final chronology estimates a decreased growth rate in the upper 200 mm of sample Wu87 (Fig. 2B and C). Across this depth, the stalagmite is mostly composed of compact calcite, and three surfaces of reduced growth can be observed (Fig. 2A), suggesting the reliability of our age model.

Isotopic records

Over the growth period, Wu87 δ^{18}O values vary from −7‰ to −8.5‰ (Fig. 2C). Two ^{18}O-depleted events centering at about 70.3 and 68.9 ka (Fig. 2C) are temporally in line with Chinese Interstadials (CIS) 19b and 19a (Cheng et al., 2006). Subsequently, δ^{18}O values gradually decrease from −7.2‰ to −8‰ during Chinese Stadial (CS) 19 (blue bar in Fig. 4), followed by a sharp jump to −8.5‰ at about 64 ka (Fig. 2C). This ^{18}O-depleted event surrounding 63 ka probably corresponds to CIS 18. Comparatively, shifts of δ^{13}C fall within a narrow range (from −3.5‰ to −4.5‰). Moreover, the δ^{13}C record is characterized by centennial-scale variability throughout MIS 4, showing a more obscure imprint of millennial-scale changes than the δ^{18}O signal. Between 71 and 68.5 ka, CIS 19b and CIS 19a in the δ^{18}O record also appear to be expressed in the δ^{13}C record. However, the long-term δ^{18}O depletion between 68 and 64 ka and CIS 18 are not expressed in the δ^{13}C record.

Growth rate of Wu87 was relatively stable in MIS 4, except during CIS 19b and before 72.6 ka (Fig. 2C, gray line). At about 70.5 ka, a sharp increase in the growth rate postdated the onset of CIS 19b, and an abrupt decrease at 69.7 ka led the end of CIS 19a. This relationship suggests that the growth rate has negligible impact on Wu87 δ^{18}O variability. In Figure 2C, maximum δ^{18}O values occur between 73 and 71 ka. At about 72.7 ka, δ^{18}O and δ^{13}C values rapidly increase to −6.3‰ and −2.7‰, respectively (Fig. 2C, gray bar). This change corresponds to the dissolutional depth spanning 429 to 436 mm (Fig. 2A). Isotopic analyses along three transects show that the results in the center deviate from those at the flank by 5 to 7 mm on average (Fig. 3). Some minor discrepancies between them are likely attributed to less precise subsample collection along a single growth layer. Hence, it is probably that at least 5- to 7-mm-thick calcite was dissolved on the central growth axis.

DISCUSSION

Environmental interpretation of isotopic records

Changes in speleothem δ^{18}O are mainly dictated by the isotopic composition of meteoric precipitation. Along the moisture trajectory, the precipitation δ^{18}O signal is further modulated by various processes, including the source effect, altitude and latitude effects, rainfall amount, surface and in-cave temperature changes, and water–rock interactions (McDermott, 2004; Fairchild et al., 2006; Lachniet, 2009). At the millennial scale, it has been suggested that speleothem δ^{18}O records

https://doi.org/10.1017/qua.2019.36 Published online by Cambridge University Press

Table 1. ^{230}Th dating results of sample Wu87 from Wulu Cave, southern China. Errors are 2σ analytical errors. Decay constant values are $\lambda_{230} = 9.1577 \times 10^{-6}$ yr^{-1}; $\lambda_{234} = 2.8263 \times 10^{-6}$ yr^{-1}; $\lambda_{238} = 1.55125 \times 10^{-10}$ yr^{-1}. Corrected ^{230}Th ages assume an initial ^{230}Th/^{232}Th atomic ratio of $(4.4 \pm 2.2) \times 10^{-6}$. Corrected ^{230}Th ages are indicated in bold and presented in thousand years before present (ka).

Sample number	Depth (mm)	^{238}U (ppb)	^{232}Th (ppt)	δ^{234}U (measured)	^{230}Th/^{238}U (activity)	^{230}Th/^{232}Th (ppm)	^{230}Th age (uncorrected)	^{230}Th age (ka) (corrected)	$\delta^{234}U_{Initial}$ (corrected)
Wu87-11	11	7619.9 ± 5.3	439.5 ± 194.2	666.0 ± 2.9	0.74975 ± 0.00125	39,715.8 ± 17540.9	62.3 ± 0.2	**62.3 ± 0.2**	793.9 ± 3.5
Wu87-92	92	10,282.6 ± 8.0	296.7 ± 190.1	659.9 ± 3.0	0.77363 ± 0.00138	81,962.7 ± 52501.6	65.2 ± 0.2	**65.2 ± 0.2**	793.1 ± 3.6
Wu87-160	160	9585.0 ± 6.8	196.7 ± 192.7	648.0 ± 3.0	0.78617 ± 0.00136	117,068.1 ± 114750.0	67.3 ± 0.2	**67.3 ± 0.3**	783.4 ± 3.7
Wu87-190	190	10,594.1 ± 8.7	427.4 ± 193.4	643.1 ± 3.2	0.79793 ± 0.00149	60,431.2 ± 27352.5	68.9 ± 0.3	**68.9 ± 0.3**	781.1 ± 3.9
Wu87-220	220	8785.4 ± 2.2	1219.9 ± 263.2	656.1 ± 1.2	0.81167 ± 0.00102	17,868.4 ± 3849.4	69.7 ± 0.1	**69.7 ± 0.1**	798.7 ± 1.4
Wu87-270	270	9084.1 ± 6.5	855.8 ± 203.7	640.6 ± 3.1	0.80365 ± 0.00153	26,069.8 ± 6203.1	69.7 ± 0.3	**69.7 ± 0.3**	779.9 ± 3.8
Wu87-330	330	10,010.0 ± 8.3	282.9 ± 196.9	644.5 ± 3.1	0.81008 ± 0.00150	87,638.3 ± 60958.9	70.2 ± 0.3	**70.2 ± 0.3**	785.7 ± 3.8
Wu87-380	380	10,007.3 ± 6.9	164.2 ± 200.4	639.6 ± 3.0	0.81032 ± 0.00145	150,796.1 ± 184179.3	70.5 ± 0.2	**70.5 ± 0.3**	780.5 ± 3.7
Wu87-428	428	7552.0 ± 2.2	664.3 ± 256.4	643.6 ± 1.1	0.82188 ± 0.00107	28,552.0 ± 11023.9	71.6 ± 0.1	**71.6 ± 0.1**	787.8 ± 1.3
Wu87-437	437	5503.5 ± 1.6	65.1 ± 217.4	641.9 ± 1.2	0.82944 ± 0.00094	213,431.1 ± 715585.2	72.6 ± 0.1	**72.6 ± 0.2**	787.9 ± 1.6
Wu87-470	470	10,657.1 ± 7.7	156.1 ± 202.9	628.9 ± 3. 2	0.82356 ± 0.00147	171,793.1 ± 222890.4	72.8 ± 0.3	**72.8 ± 0.3**	772.3 ± 3. 9
Wu87-532	532	9939.2 ± 8.7	1003.4 ± 199.2	639.0 ± 3.0	0.83574 ± 0.00154	25,301.7 ± 5025.9	73.6 ± 0.3	**73.6 ± 0.3**	786.4 ± 3.7

from the ASM area, especially from southeastern China, reflect local rainfall amounts (Cai et al., 2015), precipitation seasonality (Wang et al., 2001; Zhang et al., 2018), or ASM intensity (Cheng et al., 2006; Wang et al., 2008). The rainfall amount assumption, however, is believed to be inconsistent with other precipitation proxies from loess/paleosol magnetic properties (Maher, 2008). It is most likely that changes in the upstream circulation regime are more important (Pausata et al., 2011; Cheng et al., 2012; Maher and Thompson, 2012;Tan, 2014). Consequently, a strong southeasterly flow developing over the upstream region likely induces a strong ASM (with ^{18}O-depleted moisture). At our study site, where the summer rainfall (June through September) contributes 64% (on average) to the annual mean, it is likely that summer moisture and its isotopic composition are most important. Following this reasoning, we interpret our speleothem δ^{18}O signal as an indicator of average ASM intensity, with minimum values corresponding to a strong ASM. This explanation does not imply a reflection of rainfall amount or rainfall seasonality, but rather of changes in the average intensity of circulation regime, which transfers ^{18}O-bearing moisture from tropical oceans to the Asian continent and results in the widely observed replication in spatially separated cave records (Cheng et al., 2012; Maher and Thompson, 2012; Tan, 2014).

Carbon isotopes (δ^{13}C) in speleothems are primarily (60%–90%) derived from soil CO_2 by plant respiration and microbial decomposition (Genty et al., 2003; Meyer et al., 2014). At the Wulu site, the modern vegetation type above the cave is mainly composed of deciduous herbs. Our previous work on speleothem records from the same cave revealed a consistent coupling of centennial-scale changes in δ^{18}O and δ^{13}C (Liu et al., 2016). This suggests that the soil moisture is important for δ^{13}C variability at the centennial scale and is further supported by a recent study on δ^{13}C values of dissolved inorganic carbon in cave dripwater in southern China (Li and Li, 2018). At 72.7 ka (before the hiatus), sharp enrichments in both isotopic values (Fig. 2C) are likely a response to water deficiency at this time.

Muted ASM variability during interstadials in contrast to stadial instabilities

In Figure 4A and C, changes of Wu87 δ^{18}O and δ^{13}C during CIS 19 are characterized by weaker fluctuations (less than 0.3‰ and 0.5‰, respectively) than those in stadials. To further explore the structure of these minor oscillations, millennial-scale variability was removed using the software package ChangePoint (Killick et al., 2012). Two detrended sequences ($\delta^{18}O_d$, $\delta^{13}C_d$) reveal similar variations on a centennial time scale ($r = 0.51$, $P < 0.01$), especially during isotopic enrichment events (Fig. 4B, green bar). At the decadal scale, however, significant divergence can be observed. During stadials surrounding CIS 19, variations in $\delta^{18}O_d$ and $\delta^{13}C_d$ are about 0.4‰ and 0.8‰, respectively, almost double the changes in CIS 19. Cross-wavelet analysis between $\delta^{18}O_d$ and $\delta^{13}C_d$

https://doi.org/10.1017/qua.2019.36 Published online by Cambridge University Press

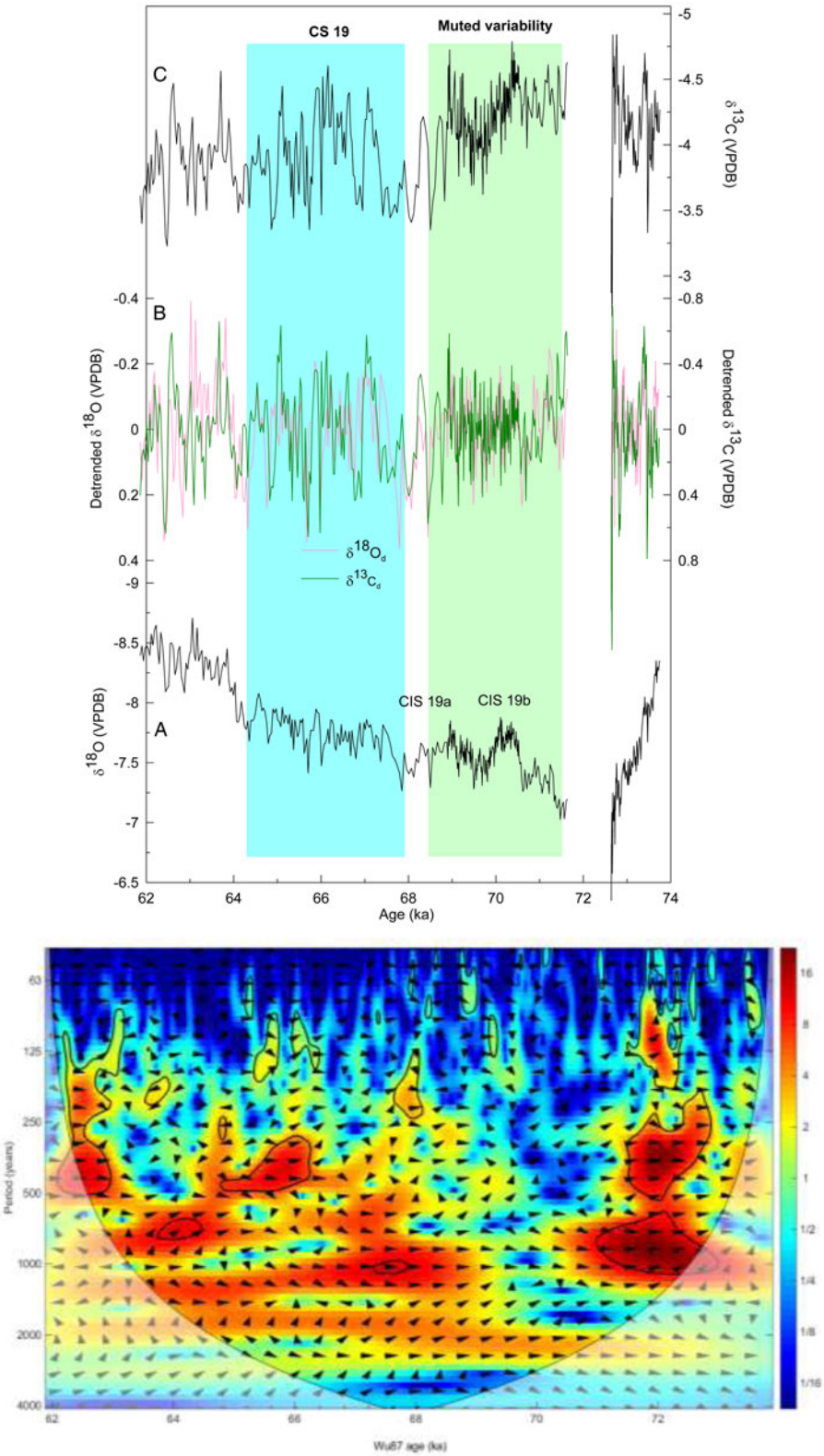

Figure 4. Comparison of original and detrended isotopic records from sample Wu87 (upper panel) and cross-wavelet analysis between detrended $\delta^{18}O$ and $\delta^{13}C$ records (lower panel). The detrended isotopic data were obtained using the software package ChangePoint (Killick et al., 2012). In the upper panel, the green bar indicates the period of muted Asian summer monsoon (ASM) variability during CIS 19, and the blue bar indicates the CS 19 interval. During CIS 19, centennial-scale ASM changes were absent in the wavelet analysis (lower panel). (For interpretation of the references to color in this figure legend, the reader is referred to the web version of this article.)

https://doi.org/10.1017/qua.2019.36 Published online by Cambridge University Press

records reveals that millennial to centennial variability is almost absent between 71.2 and 68.8 ka (Fig. 4, lower panel), supporting our visual observations.

During (peak) interstadials, weak ASM variability appears as a pervasive phenomenon in Asian speleothem records (Fig. 5) (Liu et al., 2010, 2016; Cui et al., 2012; Zhang et al., 2019). In these cave records, $\delta^{18}O_d$ records are characterized by minor (less than 0.3‰ in amplitude) and high-frequency (centennial to decadal) variability during CIS 5.1 (Fig. 5B) (Liu et al., 2016), CIS 16 (Fig. 5C) (Liu et al., 2010), and CIS 19 (Fig. 5D) (Zhang et al., 2019). Similarly, such muted variability is also reflected in coeval $\delta^{13}C_d$ records. During the stadials , changes in the $\delta^{18}O_d$ and $\delta^{13}C_d$ records increase in amplitude and decrease in frequency. Cross-wavelet analysis between these $\delta^{18}O_d$ and $\delta^{13}C_d$ sequences supports weak variability during interstadials (Supplementary Fig. 1). This suggests that limited perturbations were introduced into the ASM system and regional environments during peak interstadials. At the Medieval Warm Period (MWP)/Little Ice Age (LIA) boundary, however, a prominent change is reflected in the frequency domain of the two isotopic data sets, but not in the amplitude (Fig. 5A) (Cui et al., 2012). Especially during the MWP, large oscillations are evident in the $\delta^{13}C$ record as compared with the LIA. An increase of summer precipitation during the LIA caused by the Mei-Yu front was proposed by Cui et al. (2012). This effect of excess humidity in the LIA probably did not favor the dissolution of ^{13}C-depleted soil CO_2 in the infiltration water and led to elevated speleothem $\delta^{13}C$ values (Bar-Matthews et al., 2000; Plagnes et al., 2002).

Stable interstadial climate conditions have been identified in North Atlantic sediment records (Vautravers et al., 2004; Goñi et al., 2009) and paleolake records from western Europe (Ampel et al., 2010). Typically, summer-related indicators in these studies exhibit a pattern similar to the ASM variability observed in our study These observations possibly shed some light on climate variability in the context of current global warming. In the last millennium, severe drought events seldom occurred during warming episodes (Zhang, 2005; Hou et al., 2008), which is partly consistent with our results for interstadial conditions. Under the current warming, if the increased melting of the Greenland and Antarctic Ice Sheets (Bjørk et al., 2012; Shen et al., 2018) induces a reduction of the Atlantic meridional overturning circulation (AMOC) (Mikolajewicz et al., 2007), a stadial-like climate and significant climate extremes are likely.

Detailed correlation of high- and low-latitude climates in MIS 4

In the last glaciation, abrupt reduction in the ASM intensity at the millennial scale was thought to be in line with Greenland temperature variability (Wang et al., 2001), possibly via the westerly winds (Porter and An, 1995). Increasing evidence, however, shows that significant discrepancies can be observed between high- and low-latitude climate records. First, relatively gradual speleothem-based ASM variability was found during the late MIS 4 (Zhang et al., 2017), at the onset of CIS 12 (Cai et al., 2006), during the Bølling interstadial (Wang et al., 2001), and during the Younger Dryas (Liu et al., 2008). During these periods, the rise/fall of ASM intensity was frequently accomplished in a longer time compared with Greenland temperature variability. Second, a decoupling of the ASM and Greenland temperature variability is clear during HSs (Zhang et al., 2016; Liu et al., 2018), when the ASM is highly unstable. This suggests that the speleothem $\delta^{18}O$ signal from the Asian continent exhibits an appreciably regional feature, which is not exclusive to cave records, as ASM-type changes are widely reflected in various marine and terrestrial records (Vautravers et al., 2004; Schmidt et al., 2006; Goñi et al., 2008).

During MIS 4, double peaks in CIS 19 (19a and 19b) and a rapid depletion of 0.8‰ in $\delta^{18}O$ values at 63 ka (likely corresponding to CIS 18) in the Wu87 record (Fig. 6A) agree well, within dating uncertainties, with other cave records from China (Fig. 6B and C) (Chen et al., 2016; Zhang et al., 2019). These millennial-scale ASM oscillations, including subcycles, are also mirrored in North Greenland Ice Core Project (NGRIP) ice-core Ca^{2+} and $\delta^{18}O$ (Fig. 6D and E) (Rasmussen et al., 2014) and $\delta^{15}N$-inferred temperature records (Fig. 6F) (Kindler et al., 2014). Among these events, the short-lived cold/aridity episode between CIS 19a and CIS 19b (Fig. 6A–F, dotted lines) corresponds to a weak Antarctic warming (Fig. 6I) (Veres et al., 2013). Additionally, CIS 18 in speleothem records and its equivalents in Greenland ice-core records (Fig. 6, dotted line) register as a notable cooling in West Antarctica (Fig. 6H) (WAIS Divide Project Members, 2015), although they are weakly expressed at the EDML ice core (Fig. 6I) (Veres et al., 2013). This relationship supports a conception of interhemispheric climate changes as a bipolar seesaw (Broecker, 1998; Blunier and Brook, 2001).

Regardless of this tight interhemispheric climate link, Greenland temperatures remained in a stable cold state during Stadial 19 (Fig. 6E and F, gray bar), a climate condition similar to that during late MIS 4. At Antarctica, a rise of surface temperature initiated at about 68.9 ka (Fig. 6I, orange line), immediately after the end of Interstadial 19a. This Antarctic warming persisted throughout MIS 4 and accelerated appreciably after Interstadial 18 (Fig. 6H and I). Similarly, a gradual ASM intensification is exceptionally clear in early MIS 4 (Fig. 6B and C, gray bar), especially in our newly retrieved Wu87 record (Fig. 6A). In these speleothem records, the ASM intensity during CS 19 appears stronger on average, or is at least not weaker than during CIS 19. This pattern of ASM variability generally follows Antarctic temperature changes, but is decoupled from Greenland temperatures. Consequently, these observations show that the climate of the Southern Hemisphere and the ASM were intimately related during early MIS 4.

A southern and northern imprint on the ASM variability

The idea of an AMOC impact on the interhemispheric climate link appears valid during the interstadials, as shown in

https://doi.org/10.1017/qua.2019.36 Published online by Cambridge University Press

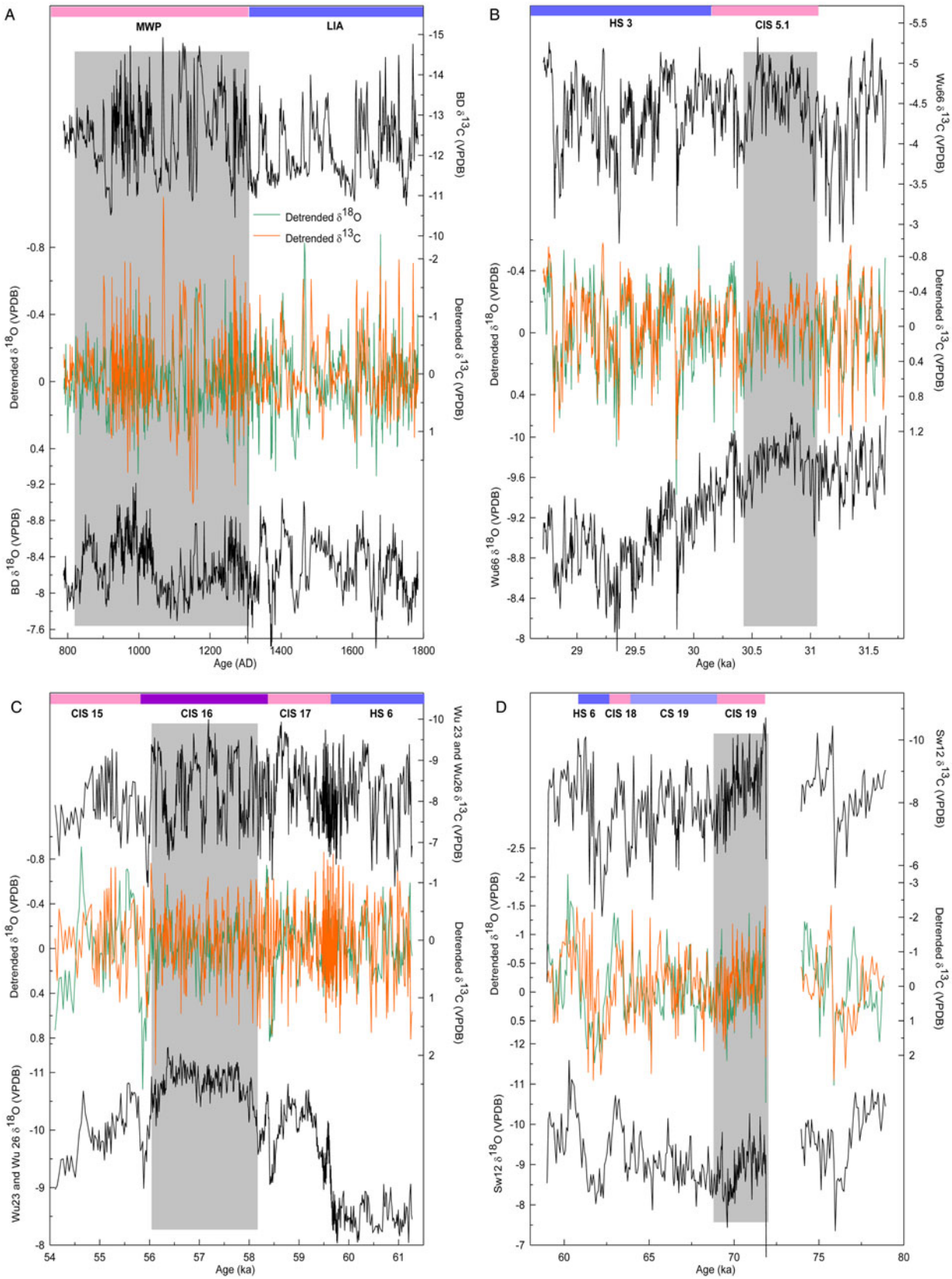

Figure 5. Correlation of intrainterstadial and intrastadial Asian summer monsoon (ASM) changes. Speleothem records from Heilong Cave, central China (A) (Cui et al., 2012), Wulu Cave, southern China (B, C) (Liu et al., 2010; 2016), and Tian'e Cave, central China (D) (Zhang et al., 2019). Gray bars in these panels indicate interstadial or peak interstadial conditions, with interstadials/stadials labeled at the top. Detrended $\delta^{18}O$ (green line) and $\delta^{13}C$ (orange line) records are shown in the middle of each panel. CIS, Chinese Interstadial; CS, Chinese Stadial; HS, Heinrich Stadial; MWP, Medieval Warm Period; LIA, Little Ice Age. (For interpretation of the references to color in this figure legend, the reader is referred to the web version of this article.)

https://doi.org/10.1017/qua.2019.36 Published online by Cambridge University Press

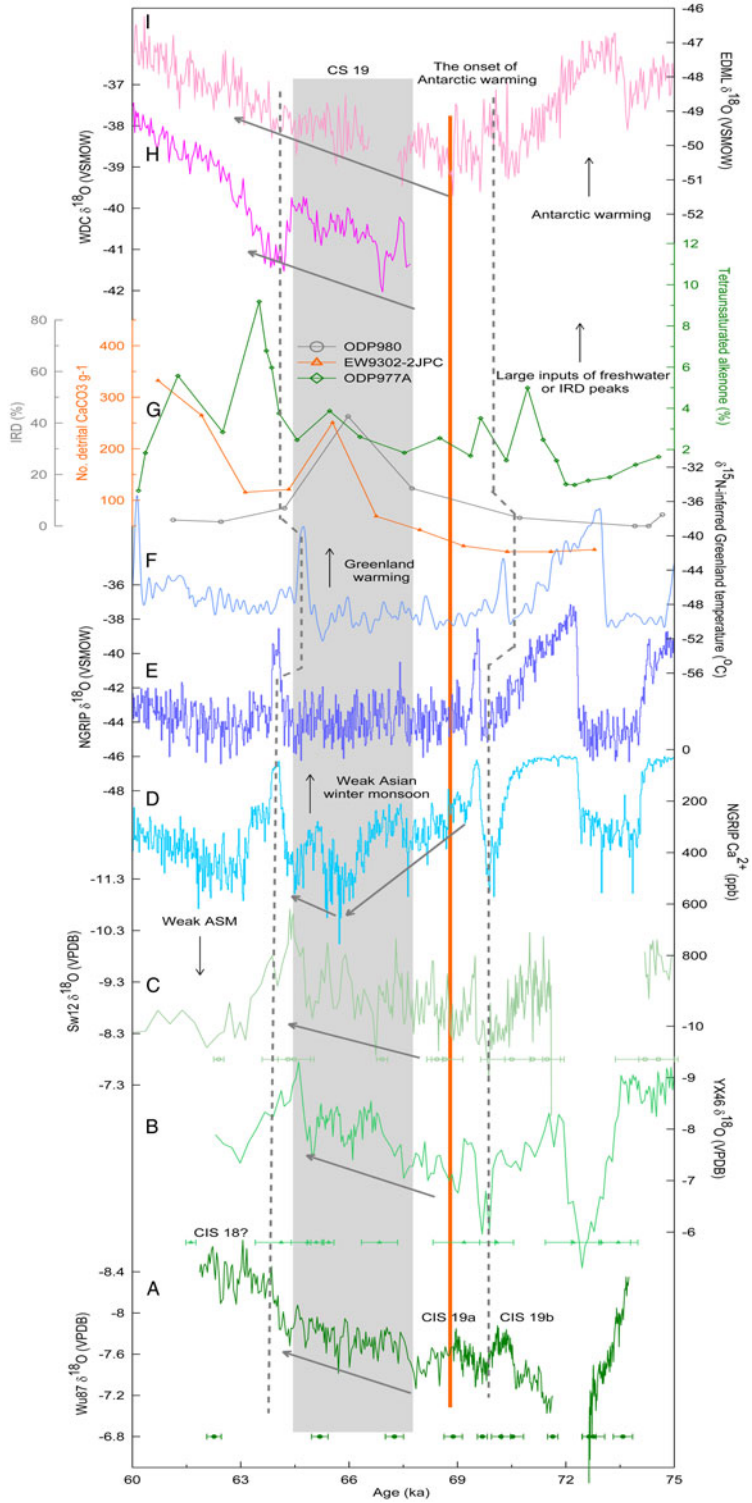

Figure 6. Climate events surrounding MIS 4. $\delta^{18}O$ records from Wulu (A) (this study), Yongxing (B; Chen et al., 2016), and Tian'e Caves (C; Zhang et al., 2019); Greenland ice-core Ca^{2+}, $\delta^{18}O$ (D, E; Rasmussen et al., 2014) and $\delta^{15}N$ records (F; Kindler et al., 2014); (G) Ice-rafted debris (IRD) is plotted as the number of detrital sediment grains (lithics) from core ODP980 (55°29′N, 14°42′W, depth of 2179 m) (gray line; McManus et al., 1999) and ice-rafted detrital $CaCO_3$ grains g^{-1} from core EW9302-2JPC (48°47.70′N, 45°05.09′W, depth of 1251 m), North Atlantic (pink line; Marcott et al., 2011); tetraunsaturated alkenone record from core ODP977A, western Mediterranean (36°1.907′N, 1°57.319′W, depth of 1984 m) is a tracer for low-salinity water masses (green line; Martrat et al., 2004); and Antarctic $\delta^{18}O$ records from the WDC (H; WAIS Divide Project Members, 2015) and EDML ice cores (I; Veres et al., 2013). The dotted lines show the correlation of interhemispheric climate changes during Interstadial 18 and the stadial between Interstadials 19a and 19b, respectively. The orange bar denotes the initiation of Antarctic warming during MIS 4, and the gray bar indicates Stadial 19 (early MIS 4). Substages of Asian summer monsoon (ASM) variability are also shown at the bottom. (For interpretation of the references to color in this figure legend, the reader is referred to the web version of this article.)

https://doi.org/10.1017/qua.2019.36 Published online by Cambridge University Press

Figure 6, where an antiphase relationship is evident. In this regard, the northern displacement of the ITCZ during southern stadials (Broccoli et al., 2006; Stouffer et al., 2006) that accompanies a strong AMOC can induce a strong ASM and more precipitation in southern China (Wang et al., 2006). Thus, a more stable ASM during CIS, as derived from our speleothem records (Fig. 5), likely points to an average northerly positioned ITCZ. In contrast, in northern stadials, the frequent intrusion of a northern high-pressure system, including a southerly positioned ITCZ, could have reduced ASM intensity and triggered ASM instabilities (Webster et al., 1998; Wang et al., 2014, 2017; An et al., 2015) when the AMOC was weak and frigid cold returned to the northern high latitudes.

During MIS 4, peaks of ice-rafted debris (IRD) from limited-resolution oceanic sediment records suggest catastrophic iceberg and freshwater discharges into the North Atlantic occurred at about 66 ka (Fig. 6G, gray and orange lines) (McManus et al., 1999; Marcott et al., 2011). Additionally, a high-resolution alkenone record from core ODP977A indicates that a large volume of low-salinity water masses intruded into the western Mediterranean at about 64 ka (Fig. 6G, green line) (Martrat et al., 2004). Taking the dating uncertainties of these oceanic sediment records into consideration,, these lines of evidence show that a significant AMOC reduction most likely occurred in late MIS 4 (HS 6), as summarized in Hemming (2004). Accordingly, Greenland temperature (Fig. 6E and F) (Kindler et al., 2014; Rasmussen et al., 2014) and ASM intensity declined significantly after Interstadial 18 (Fig. 6C, arrowed line) (Chen et al., 2016; Zhang et al., 2019). In response to the interhemispheric thermal gradient caused by freshwater perturbations, a southerly positioned ITCZ and an accelerated Antarctic warming would be expected (Fig. 6H and I) (Veres et al., 2013; WAIS Divide Project Members, 2015).

Nevertheless, this idea of latitudinal shifts in the ITCZ (in a scenario of freshwater impact) lacks validity regarding synchronous increase in the ASM intensity and Antarctic temperature in early MIS 4 (CS 19) (Fig. 6), because IRD peaks for that time period were insignificant (Fig. 6G). One possibility for the coupling of ASM and Antarctic temperature is an expansion of the ITCZ (Collins et al., 2011; Yan et al., 2015; Denniston et al., 2016). In early MIS 4, the Mg/Ca-based summertime sea-surface temperatures (SSTs), reconstructed from *Globigerinoides ruber* records from the western tropical Pacific (6.3°N, 125.83°E), were relatively stable (generally above 28°C) (Stott et al., 2002). This implies that thermal conditions in the Indo-Pacific Warm Pool (IPWP) were favorable for ITCZ expansion at this time, as a rise in SST to 27.5°C is required for initiation of deep convection (Graham and Barnett, 1987). ITCZ position is sensitive to slight shifts in the atmospheric energy balance. Currently, the hemispherically asymmetric contrast of mid-tropospheric temperatures is less than 3 Kelvin in the zonal mean between 20°N and 20°S (Schneider et al., 2014). It is believed that a gradient of 1 Kelvin between high- and low-latitude SSTs could trigger the displacement of the ITCZ (Hastenrath and Heller, 1977). Moreover, other sediment records have shown that the tropical Pacific SST in early MIS 4 reached its average modern value (22°C to 29°C), with centennial-scale changes falling within the seasonal range of 2°C (Fig. 7C) (Rosenthal et al., 2003; Lea et al., 2000, 2006). A significant warming of about 2°C was also registered at the midlatitudes of the southern Pacific (Fig. 7B) (Pahnke and Sachs, 2006; Tachikawa et al., 2009) and the South China Sea (Fig. 7D) (Oppo and Sun, 2005). This SST variability is in line with the gradual increase in ASM intensity in our speleothem record (Fig. 7A). Consequently, the concurrent increase in ASM intensity and Antarctic temperature (Fig. 6, orange line) should reflect an expansion of ITCZ when freshwater discharges ceased.

Hence, the thermal contrast between the two hemispheres is very important. We speculate that when the AMOC is exceptionally strong (or weak), a large interhemispheric thermal gradient would result in a latitudinal migration of the ITCZ, as demonstrated by modeling studies (Broccoli et al., 2006; Stouffer et al., 2006). This could explain the antiphase relationship between the ASM and Antarctic temperature during Interstadials 19 and 18 and late MIS 4 (Fig. 6). In contrast, a small thermal gradient between the two hemispheres is favorable for an expansion/contraction of the ITCZ, which is partly reminiscent of the concurrent rise in the ASM strength and Antarctic temperature during early MIS 4. This simplified concept of ocean–atmosphere response is probably similar to the mechanism associated with triple AMOC states, that is, a glacial mode, a Heinrich mode, and a modern mode (Clark et al., 2002), which is further modulated by ice-shelf and sea-ice interactions (Boers et al., 2018). It is currently out of our scope to evaluate the northernmost boundary of the ITCZ. Our comparison suggests that the impact of the ITCZ is probably limited to mid- to low latitudes, as an increase in NGRIP ice-core Ca^{2+} concentration (indicating a strong Asian winter monsoon) can be observed before the onset of Interstadial 18 (Fig. 6D) (Rasmussen et al., 2014). In our speleothem records, the ASM intensification persisted throughout early MIS 4 (Fig. 6A–C, gray bar). A decoupling of ASM intensity and Greenland temperature was also observed during mid-HS (Liu et al., 2018). In this study, speleothem records from central to southern China revealed a gradual ASM intensification in mid-HS, in stark contrast to a stable cold climate state in Greenland. It is probably a reflection of the impact of low-latitude hydrothermal processes.

These observations are of vital importance for understanding the dynamics of millennial-scale climate changes, because the frequency and amplitude of interstadials/stadials are controlled by North Atlantic processes, and their magnitude increases with increasing latitude (Masson-Delmotte et al., 2011; Shakun et al., 2012; Cuffey et al., 2016). However, the evolution and duration of millennial-scale climate events, especially within northern low latitudes, is probably determined by southern oceanic processes (Buizert and Schmittner, 2015). In Asian speleothem records, gradual $\delta^{18}O$ variability can be expected at CIS/CS transitions in contrast to abrupt changes in Greenland temperature (Wang et al.,

https://doi.org/10.1017/qua.2019.36 Published online by Cambridge University Press

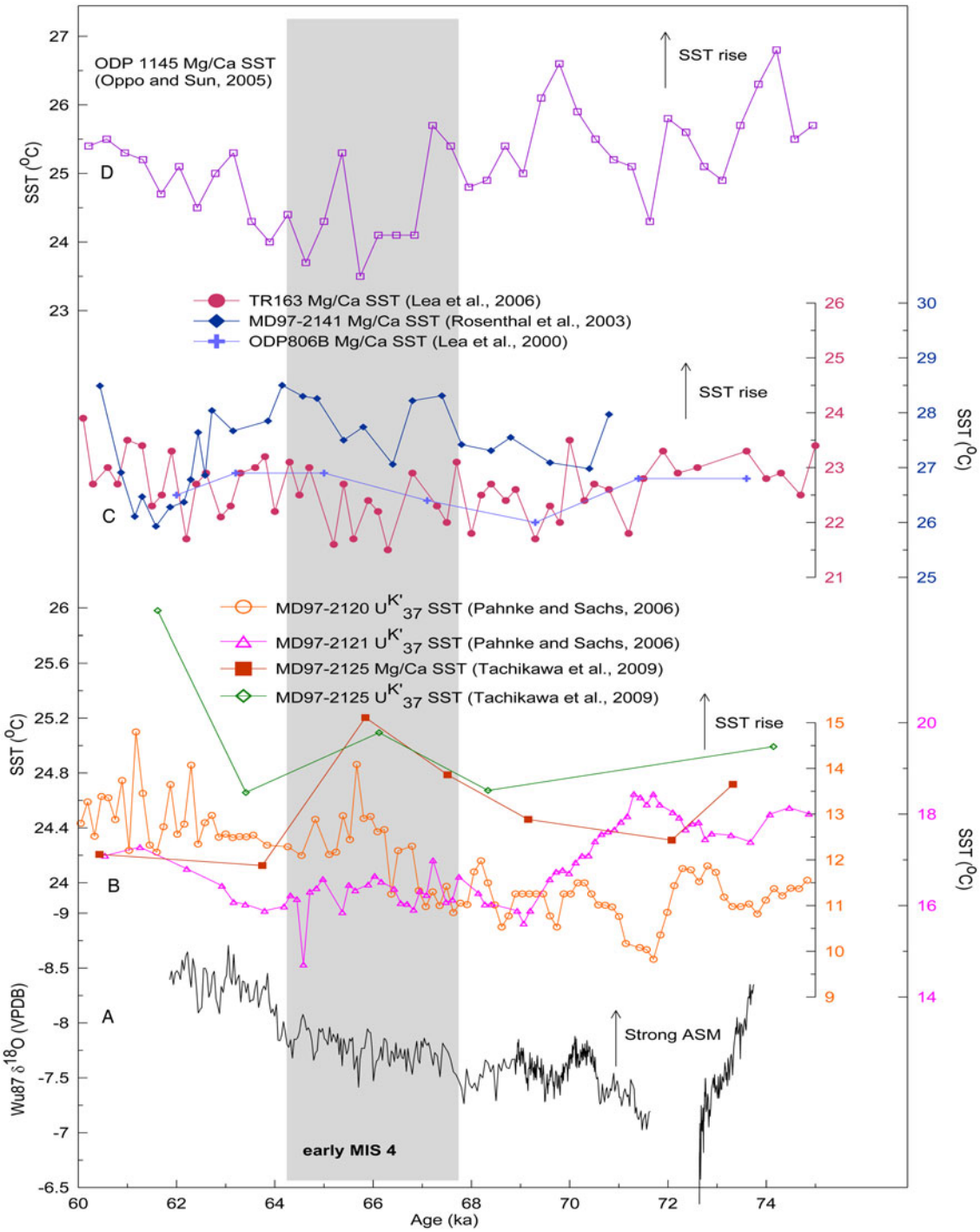

Figure 7. (Color online) Dynamic link of Asian summer monsoon (ASM) changes and sea-surface temperature (SST) records in MIS 4. (A) Wu87 $\delta^{18}O$ record (this study); (B) SST changes at subtropical southern Pacific (MD97-2120 [45°32.06′S, 174°55.85′E] and MD97-2121 [40°22.8′S, 177° 59.4′E]; Pahnke and Sachs, 2006; MD2125 [22°34′S, 161°44′E]; Tachikawa et al., 2009); (C) IPWP SST (ODP806B [0°19.04′N, 159°21.25′E]; Lea et al., 2000; TR163 [0°30.9′N, 92°23.9′W]; Lea et al., 2006; MD97-2141 [8.8°N, 121.3°E]; Rosenthal et al., 2003); (D) SST changes at the South China Sea (ODP1145 [19°35′N, 117°38′E]; Oppo and Sun, 2005). Gray bar indicates early MIS 4, when SST in each site reached its modern level.

2001; Cai et al., 2006; Liu et al., 2008, 2018; Zhang et al., 2017). Sensitive to the interhemispheric temperature gradient, the ITCZ can act a bridge to link bipolar climates via expansion/contraction and "pull–push" mechanisms (Rohling et al., 2009). Therefore, one needs to precisely pinpoint the "zero-anomaly line" of the interhemispheric thermal gradient in the past (Stouffer et al., 2006; Zarriess et al., 2011). Within the IPWP, a sharp precipitation boundary between the maritime continents and Australia was located at about 8–10° S during the last termination (Lo et al., 2014); however, a

https://doi.org/10.1017/qua.2019.36 Published online by Cambridge University Press

geographic mismatch between meridional thermal and rainfall patterns (Linsley et al., 2010) suggests that the zero-anomaly line variability deserves further investigation, especially at contrasting climate boundaries.

CONCLUSIONS

A high-resolution speleothem $\delta^{18}O$ record from southern China presents a detailed ASM history spanning CIS 19 to the onset of CIS 18. During these interstadials and late MIS 4, ASM variations were in line with millennial-scale changes in northern high-latitude temperatures derived from Greenland ice-core $\delta^{18}O$ (Rasmussen et al., 2014) and $\delta^{15}N$ records (Kindler et al., 2014), but antiphased with Antarctic climates. In early MIS 4, however, an increase in ASM intensity can be observed just after CIS 19, in agreement with a rise in Antarctic temperature. At the centennial scale, the ASM was stable during peak interstadials, while significant instabilities were evident in stadials. In the antiphase scenario (i.e., CIS 19, CIS 18, and late MIS 4), latitudinal shifts of the ITCZ might dominate, as large freshwater discharges can be found in late MIS 4. In an in-phase case, a symmetrical expansion/contraction of the ITCZ would be expected. Consequently, we speculate that an expansion/contraction mode is important for ITCZ movement when freshwater perturbations are negligible (Collins et al., 2011; Yan et al., 2015; Denniston et al., 2016).

ACKNOWLEDGMENTS

We are grateful to three anonymous reviewers for their generous technical comments on an early version of this manuscript. This work was jointly supported by grants from the National Nature Science Foundation of China (no. 41672161), a project funded by the Priority Academic Program Development of Jiangsu Higher Education Institutions (164320H116), the Jiangsu Center for Collaborative Innovation in Geographical Information Resource Development and Application, and the Key Laboratory of Virtual Geographic Environments (Nanjing Normal University).

SUPPLEMENTARY MATERIAL

The supplementary material for this article can be found at https://doi.org/10.1017/qua.2019.36

REFERENCES

Ampel, L., Bigler, C., Wohlfarth, B., Risberg, J., Lotter, A.F., Veres, D., 2010. Modest summer temperature variability during DO cycles in western Europe. *Quaternary Science Reviews* 29, 1322–1327.

An, Z.S., Wu, G.X., Li, J.P., Sun, Y.B., Liu, Y.M., Zhou, W.J., Cai, Y.J., *et al*., 2015. Global monsoon dynamics and climate change. *Annual Review of Earth and Planetary Sciences* 43, 29–77.

Bar-Matthews, M., Ayalon, A., Kaufman, A., 2000. Timing and hydrological conditions of Sapropel events in the Eastern Mediterranean, as evident from speleothems, Soreq cave, Israel. *Chemical Geology* 169, 145–156.

Bjørk, A.A., Kjær, K.H., Korsgaard, N.J., Khan, S.A., Kjeldsen, K.K., Andresen, C.S., Box, J.E., Larsen, N.K., Funder, S., 2012. An aerial view of 80 years of climate-related glacier fluctuations in southeast Greenland. *Nature Geoscience* 5, 427–432.

Blunier, T., Brook, E.J., 2001. Timing of millennial-scale climate change in Antarctica and Greenland during the last glacial period. *Science* 291, 109–112.

Boers, N., Ghil, M., Rousseau, D.-D., 2018. Ocean circulation, ice shelf, and sea ice interactions explain Dansgaard-Oeschger cycles. *Proceedings of the National Academy of Sciences USA* 115, E11005–E11014.

Broccoli, A.J., Dahl, K.A., Stouffer, R.J., 2006. Response of the ITCZ to Northern Hemisphere cooling. *Geophysical Research Letters* 33, L01702.

Broecker, W.S., 1998. Paleocean circulation during the last deglaciation: a bipolar seesaw? *Paleoceanography* 13, 119–121.

Buizert, C., Schmittner, A., 2015. Southern Ocean control of glacial AMOC stability and Dansgaard-Oeschger interstadial duration. *Paleoceanography* 30. http://dx.doi.org/10.1002/2015PA002795.

Cai, Y.J., An, Z.S., Cheng, H., Edwards, R.L., Kelly, M.J., Liu, W.G., Wang, X.F., Shen, C.-C., 2006. High-resolution absolute-dated Indian Monsoon record between 53 and 36 ka from Xiaobailong Cave, southwestern China. *Geology* 34, 621–624.

Cai, Y.J., Fung, I.Y., Edwards, R.L., An, Z.S., Cheng, H., Lee, J.-E., Tan, L.C., *et al*., 2015. Variability of stalagmite-inferred Indian monsoon precipitation over the past 252,000 y. *Proceedings of the National Academy of Sciences USA* 112, 2954–2959.

Chen, S. T., Wang, Y. J., Cheng, H., Edwards, R. L., Wang, X. F., Kong, X. G., Liu, D. B., 2016. Strong coupling of Asian Monsoon and Antarctic climates on sub-orbital timescales, *Scientific Reports* 6, 32995.

Cheng, H., Edwards, R.L., Wang, Y.J., Kong, X.G., Ming, Y.F., Kelly, M.J., Wang, X.F., Gallup, C.D., Liu, W.G., 2006. A penultimate glacial monsoon record from Hulu Cave and two-phase glacial terminations. *Geology* 34, 217–220.

Cheng, H., Edwards, R.L., Shen, C.-C., Polyak, V.J., Asmerom, Y., Woodhead, J., Hellstrom, J., *et al*., 2013. Improvements in ^{230}Th dating, ^{230}Th and ^{234}U half-life values, and U-Th isotopic measurements by multi-collector inductively coupled plasma mass spectrometry. *Earth and Planetary Science Letters* 371–372, 82–91.

Cheng, H., Sinha, A., Wang, X.F., Cruz, F.W., Edwards, R.L., 2012. The global paleomonsoon as seen through speleothem records from Asia and the Americas. *Climate Dynamics* 39, 1045–1062.

Clark, P.U., Pisias, N.G., Stocker, T.F., Weaver, A.J., 2002. The role of the thermohaline circulation in abrupt climate change. *Nature* 415, 863–869.

Collins, J.A., Schefuß, E., Heslop, D., Mulitza, S., Prange, M., Zabel, M., Tjallingii, R., *et al*., 2011. Interhemispheric symmetry of the tropical African rainbelt over the past 23,000 years. *Nature Geoscience* 4, 42–45.

Cuffey, K.M., Clow, G.D., Steig, E.J., Buizert, C., Fudge, T.J., Koutnik, M., Waddington, E.D., Alley, R.B., Severinghaus, J.P., 2016. Deglacial temperature history of West Antarctica. *Proceedings of the National Academy of Sciences USA* 113, 14249–14254.

Cui, Y.F., Wang, Y.J., Cheng, H., Zhao, K., Kong, X.G., 2012. Isotopic and lithologic variations of one precisely-dated stalagmite

across the Medieval/LIA period from Heilong Cave, central China. *Climate of the Past* 8, 1541–1550.

Denniston, R.F., Ummenhofer, C.C., Wanamaker, A.D., Jr., Lachniet, M.S., Villarini, G., Asmerom, Y., Polyak, V.J., *et al*., 2016. Expansion and contraction of the Indo-Pacific tropical rain belt over the last three millennia. *Scientific Reports* 6. http://dx.doi.org/10.1038/srep34485.

Donohoe, A., Marshall, J., Ferreira, D., McGee, D., 2013. The relationship between ITCZ location and cross-equatorial atmospheric heat transport: from the seasonal cycle to the Last Glacial Maximum. *Journal of Climate* 26, 3597–3618.

Fairchild, I.J., Smith, C.L., Baker, A., Fuller, L., Spötl, C., Mattey, D., McDermott, F., 2006. Modification and preservation of environmental signals in speleothems. *Earth-Science Reviews* 75, 105–153.

Genty, D., Blamart, D., Ouahdi, R., Gilmour, M., Baker, A., Jouzel, J., Van-Exter, S., 2003. Precise dating of Dansgaard-Oeschger climate oscillations in western Europe from stalagmite data. *Nature* 421, 833–837.

Goñi, M.F.S., Landais, I., Cacho, I., Duprat, J., Rossignol, L., 2009. Contrasting intrainterstadial climatic evolution between high and middle North Atlantic latitudes: a close-up of Greenland Interstadials 8 and 12. *Geochemistry, Geophysics, Geosystems* 10. http://dx.doi.org/10.1029/2008GC002369.

Goñi, M.F.S., Landais, A., Fletcher, W., Naughton, F., Desprat, S., Duprat, J., 2008. Contrasting impacts of Dansgaard-Oeschger events over a western European latitudinal transect modulated by orbital parameters. *Quaternary Science Reviews* 27, 1136–1151.

Graham, N.E., Barnett, T.P., 1987. Sea surface temperature, surface wind divergence, and convection over tropical oceans. *Science* 238, 657–659.

Hastenrath, S., Heller, L., 1977. Dynamics of climatic hazards in northeast Brazil. *Quaternary Journal of the Royal Meteorological Society* 103, 79–92.

Hemming, S.R., 2004. Heinrich events: massive late Pleistocene detritus layers of the North Atlantic and their global climate imprint. *Review of Geophysics* 42, RG1005.

Hou, W., Yang, P., Feng, G.-L., 2008. The decadal variability and its cause of the extreme drought in China [in Chinese]. *Acta Physica Sinica* 57, 3932–3940.

Jacobel, A.W., MacManus, J.F., Anderson, R.F., Winckler, G., 2016. Large deglacial shifts of the Pacific Intertropical Convergence Zone. *Nature Communications* 7:10449.

Kalnay, E., Kanamitsu, M., Kistler, R., Collins, W., Deaven, D., Gandin, L., Iredell, M., *et al*., 1996. The NCEP/NCAR 40-year reanalysis project. *Bulletin of American Meteorological Society* 77, 437–71.

Killick, R., Fearnhead, P., Eckley, I.A., 2012. Optimal detection of Changepoints with a linear computational cost. *Journal of the American Statistical Association* 107, 1590–1598.

Kindler, P., Guillevic, M., Baumgartner, M., Schwander, J., Landais, A., Leuenberger, M., 2014. Temperature reconstruction from 10 to 120 kyr b2k from the NGRIP ice core. *Climate of the Past* 10, 887–902.

Lachniet, M.S., 2009. Climatic and environmental controls on speleothem oxygen-isotope values. *Quaternary Science Reviews* 28, 412–423.

Lea, D.W., Pak, D.K., Belanger, C.L., Spero, H.J., Hall, M.A., Shackleton, N.J., 2006. Paleoclimate history of Galápagos surface waters over the last 135,000 yr. *Quaternary Science Reviews* 25, 1152–1167.

Lea, D.W., Pak, D.K., Spero, H.J., 2000. Climate impact of late Quaternary equatorial Pacific sea surface temperature variations. *Science* 289, 1719–1724.

Li, J.-Y., Li, T.-Y., 2018. Seasonal and annual changes in soil/cave air pCO_2 and the $\delta^{13}C_{DIC}$ of cave drip water in response to changes in temperature and rainfall. *Applied Geochemistry* 93, 94–101.

Linsley, B.K., Rosenthal, Y., Oppo, D.W., 2010. Holocene evolution of the Indonesian throughflow and the western Pacific warm pool. *Nature Geoscience* 3, 578–583.

Liu, D.B., Wang, Y.J., Cheng, H., Edwards, R.L., Kong, X.G., Chen, S.T., Liu, S.S., 2018. Contrasting patterns in abrupt Asian summer monsoon changes in the last glacial period and the Holocene. *Paleoceanography and Paleoclimatology* 33, 214–226.

Liu, D.B., Wang, Y.J., Cheng, H., Edwards, R.L., Kong, X.G., Li, T.-Y., 2016. Strong coupling of centennial-scale changes of Asian monsoon and soil processes derived from stalagmite $\delta^{18}O$ and $\delta^{13}C$ records, southern China. *Quaternary Research* 85, 333–346.

Liu, D.B., Wang, Y.J., Cheng, H., Edwards, R.L., Kong, X.G., Wang, X.F., Hardt, B., *et al*., 2010. Sub-millennial variability of Asian monsoon intensity during the early MIS 3 and its analogue to the ice age terminations. *Quaternary Science Reviews* 29, 1107–1115.

Liu, D.B., Wang, Y.J., Cheng, H., Edwards, R.L., Kong, X.G., Wang, X.F., Wu, J.Y., Chen, S.T., 2008. A detailed comparison of Asian monsoon intensity and Greenland temperature during the Allerød and Younger Dryas events. *Earth and Planetary Science Letters* 272, 691–697.

Lo, L., Shen, C.-C., Wei, K.-Y., Burr, G.S., Mii, H.-S., Chen, M.-T., Lee, S.-Y., Tsai, M.-C., 2014. Millennial meridional dynamics of the Indo-Pacific Warm Pool during the last termination. *Climate of the Past* 10, 2253–2261.

Maher, B.A., 2008. Holocene variability of the East Asian summer monsoon from Chinese cave records: a re-assessment. *The Holocene* 18, 861–866.

Maher, B.A., Thompson, R., 2012. Oxygen isotopes from Chinese caves: records not of monsoon rainfall but of circulation regime. *Journal of Quaternary Science* 27, 615–624.

Marcott, S.A., Clark, P.U., Padman, L., Klinkhammer, G.P., Springer, S.R., Liu, Z.Y., Otto-Bliesner, B.L., *et al*., 2011. Ice-shelf collapse from subsurface warming as a trigger for Heinrich events. *Proceedings of the National Academy of Sciences USA* 108, 13415–13419.

Martrat, B., Grimalt, J.O., Lopez-Martinez, C., Cacho, I., Sierro, F.J., Flores, J.A., Zahn, R., Canals, M., Curtis, J.H., Hodell, D.A., 2004. Abrupt temperature changes in the western Mediterranean over the past 250,000 years. *Science* 306, 1762–1765.

Masson-Delmotte, V., Buiron, D., Ekaykin, A., Frezzotti, M., Gallée, H., Jouzel, J., Krinner, G., *et al*., 2011. A comparison of the present and last interglacial periods in six Antarctic ice cores. *Climate of the Past* 7, 397–423.

McDermott, F., 2004. Palaeo-climate reconstruction from stable isotope variations in speleothems: a review. *Quaternary Science Reviews* 23, 901–918.

McGee, D., Donohoe, A., Marshall, J., Ferreira, D., 2014. Changes in ITCZ location and cross-equatorial heat transport at the Last Glacial Maximum, Heinrich Stadial 1, and the mid-Holocene. *Earth and Planetary Science Letters* 390, 69–79.

McGee, D., Moreno-Chamarro, E., Green, B., Marshall, J., Galbraith, E., Bradtmiller, L., 2018. Hemispherically asymmetric

https://doi.org/10.1017/qua.2019.36 Published online by Cambridge University Press

trade wind changes as signatures of past ITCZ shifts. *Quaternary Science Reviews* 180, 214–228.

McManus, J.F., Oppo, D.W., Cullen, J.L., 1999. A 0.5-million-year record of millennial-scale climate variability in the North Atlantic. *Science* 283, 971–975.

Meyer, K.W., Feng, W., Breecker, D.O., Banner, J.L., Guifoyle, A., 2014. Interpretation of speleothem calcite $\delta^{13}C$ variations: evidence from monitoring soil CO_2, drip water, and modern speleothem calcite in central Texas. *Geochimica et Cosmochimica Acta* 142, 281–298.

Mikolajewicz, U., Gröger, M., Maier-Reimer, E., Schurgers, G., Vizcáno, M., Winguth, A.M.E., 2007. Long-term effects of anthropogenic CO_2 emissions simulated with a complex earth system model. *Climate Dynamics* 28, 599–633.

Oppo, D.W., Sun, Y.B., 2005. Amplitude and timing of sea-surface temperature change in the northern South China Sea: dynamic link to the East Asian monsoon. *Geology* 33, 785–788.

Pahnke, K., Sachs, J.P., 2006. Sea surface temperatures of southern midlatitudes 0–160 kyr B.P. *Paleoceanography* 21. http://dx.doi.org/10.1029/2005PA001191.

Pausata, F.S., Battisti, D.S., Nisancioglu, K.H., Bitz, C.M., 2011. Chinese stalagmite $\delta^{18}O$ controlled by changes in the Indian monsoon during a simulated Heinrich event. *Nature Geoscience* 4, 474–480.

Plagnes, V., Causse, C., Genty, D., Paterne, M., Blamart, D., 2002. A discontinuous climate record from 187 to 74 ka from a speleothem of the Clamouse Cave (south of France). *Earth and Planetary Science Letters* 201, 87–103.

Porter, S.C., An, Z.S., 1995. Correlation between climate events in the North Atlantic and China during the last glaciation. *Nature* 375, 305–308.

Railsback, L.B., Akers, P.D., Wang, L.X., Holdridge, G.A., Voarintsoa, N.R., 2013. Layer-bounding surfaces in stalagmites as keys to better paleoclimatological histories and chronologies. *International Journal of Speleology* 42, 167–180.

Rasmussen, S.O., Bigler, M., Blockley, S.P., Blunier, T., Buchardt, S.L., Clausen, H.B., Cvijanovic, I., *et al*., 2014. A stratigraphic framework for abrupt climatic changes during the Last Glacial period based on three synchronized Greenland ice-core records: refining and extending the INTIMATE event stratigraphy. *Quaternary Science Reviews* 106, 14–28.

Reimi, M.A., Marcantonio, F., 2016. Constrains on the magnitude of the deglacial migration of the ITCZ in the Central Equatorial Pacific Ocean. *Earth and Planetary Science Letters* 453, 1–8.

Rohling, E.J., Liu, Q.S., Roberts, A.P., Stanford, J.D., Rasmussen, S.O., Langen, P.L., Siddall, M., 2009. Controls on the East Asian monsoon during the last glacial cycle, based on comparison between Hulu Cave and polar ice-core records. *Quaternary Science Reviews* 28, 3291–3302.

Rosenthal, Y., Oppo, D.W., Linsley, B.K., 2003. The amplitude and phasing of climate change during the last deglaciation in the Sulu Sea, western equatorial Pacific. *Geophysical Research Letters* 30. http://dx.doi.org/10.1029/2002GL016612.

Sachs, J.P., Sachse, D., Smittenberg, R.H., Zhang, Z.H., Battisti, D.S., Golubic, S., 2009. Southward movement of the Pacific intertropical convergence zone AD 1400–1850. *Nature Geoscience* 2, 519–525.

Schmidt, M.W., Vautravers, M.J., Spero, H.J., 2006. Rapid subtropical North Atlantic salinity oscillations across Dansgaard-Oeschger cycles. *Nature* 443, 561–564.

Schneider, T., Bischoff, T., Haug, G.H., 2014. Migrations and dynamics of the intertropical convergence zone. *Nature* 513, 45–53.

Shakun, J.D., Clark, P.U., Marcott, S.A., Mix, A.C., Liu, Z.Y., Otto-Bliesner, B., Schmittner, A., Bard, E., 2012. Global warming preceded by increasing carbon dioxide concentrations during the last deglaciation. *Nature* 484, 49–54.

Shao, Q.F., Pons-Branchu, E., Zhu, Q.P., Wang, W., Valladas, H., Fontugne, M., 2017. High precision U/Th dating of the rock paintings at Mt. Huashan, Guangxi, southern China. *Quaternary Research* 88, 1–33.

Shen, Q., Wang, H.S., Shum, C.K., Jiang, L.M., Hsu, H.T., Dong, J.L., 2018. Recent high-resolution Antarctic ice velocity maps reveal increased mass loss in Wilkes Land, East Antarctica. *Scientific Reports* 8:4477.

Steffensen, J.P., Andersen, K.K., Bigler, M., Clausen, H.B., Dahl-Jensen, D., Fischer, H., Goto-Azuma, K., *et al*., 2008. High-resolution Greenland ice core data show abrupt climate change happens in few years. *Science* 321, 680–684.

Stott, L., Poulsen, C., Lund, S., Thunell, R., 2002. Super ENSO and global climate oscillations at millennial time scales. *Science* 297, 222–226.

Stouffer, R.J., Yin, J., Gregory, J.M., Dixon, K.W., Spelman, M.J., Hurlin, W., Weaver, A.J., *et al*., 2006. Investigating the causes of the response of the thermohaline circulation to past and future climate changes. *Journal of Climate* 19, 1365–1387.

Tachikawa, K., Vidal, L., Sonzogni, C., Bard, E., 2009. Glacial/interglacial sea surface temperature changes in the Southwest Pacific ocean over the past 360 ka. *Quaternary Science Reviews* 28, 1160–1170.

Tan, M., 2014. Circulation effect: response of precipitation $\delta^{18}O$ to the ENSO cycle in monsoon regions of China. *Climate Dynamics* 42, 1067–1077.

Thomas, E.R., Wolff, E.W., Mulvaney, R., Johnsen, S.J., Steffensen, J.P., Arrowsmith, C., 2009. Anatomy of a Dansgaard-Oeschger warming transition: high-resolution analysis of the North Greenland Ice Core Project ice core. *Journal of Geophysical Research* 114, D08102.

Vautravers, M., Shackleton, N.J., Lopez-Martinez, C., Grimalt, J.O., 2004. Gulf Stream variability during marine isotope stage 3. *Paleoceanography* 19, PA2011.

Veres, D., Bazin, L., Landais, A., Kele, H.T.M., Lemieux-Dudon, B., Parrenin, F., Martinerie, P., *et al*., 2013. The Antarctic ice core chronology (AICC2012): an optimized multi-parameter and multi-site dating approach for the last 120 thousand years. *Climate of the Past* 9, 1733–1748.

WAIS Divide Project Members, 2015. Precise interpolar phasing of abrupt climate change during the last ice age. *Nature* 520, 661–665.

Wang, P.X., Wang, B., Cheng, H., Fasullo, J., Guo, Z.T., Kiefer, T., Liu, Z.Y., 2014. The global monsoon across timescales: coherent variability of regional monsoons. *Climate of the Past* 10, 2007–2052.

Wang, P.X., Wang, B., Cheng, H., Fasullo, J., Guo, Z.T., Kiefer, T., Liu, Z.Y., 2017. The global monsoon across time scales: mechanisms and outstanding issues. *Earth-Science Reviews* 174, 84–121.

Wang, X.F., Auler, A.S., Edwards, R.L., Cheng, H., Ito, E., Solheid, M., 2006. Interhemispheric anti-phasing of rainfall during the last glacial period. *Quaternary Science Reviews* 25, 3391–3403.

Wang, Y.J., Cheng, H., Edwards, R.L., An, Z.S., Wu, J.Y., Shen, C.-C., Dorale, J.A., 2001. A high-resolution absolute-dated late Pleistocene monsoon record from Hulu Cave, China. *Science* 294, 2345–2348.

Wang, Y.J., Cheng, H., Edwards, R.L., Kong, X.G., Shao, X.H., Chen, S.T., Wu, J.Y., Jiang, X.Y., Wang, X.F., An, Z.S., 2008. Millennial- and orbital-scale changes in the East Asian monsoon over the past 224,000 years. *Nature* 451, 1090–1093.

Webster, P.J., Magaña, V.O., Palmer, T.N., Shukla, J., Tomas, R.A., Yanai, M., Yasunari, T., 1998. Monsoons: processes, predictability, and the prospects for prediction. *Journal of Geophysical Research* 103, 14,451–14,510.

Yan, H., Wei, W., Soon, W., An, Z.S., Zhou, W.J., Liu, Z.H., Wang, Y.H., Carter, R.M., 2015. Dynamics of the intertropical convergence zone over the western Pacific during the Little Ice Age. *Nature Geoscience* 8, 315–320.

Zarriess, M., Johnstone, H., Prange, M., Steph, S., Groeneveld, J., Mulitza, S., Machensen, A., 2011. Bipolar seesaw in the northeastern tropical Atlantic during Heinrich stadials. *Geophysical Research Letters* 38, L04706.

Zhang, D.E., 2005. Severe drought events as recorded in the climate records of China and their temperature situations over the last 1000 years. *Acta Meteorologica Sinica* 19, 485–491.

Zhang, H.B., Griffiths, M.L., Huang, J.H., Cai, Y.J., Wang, C.F., Zhang, F., Cheng, H., Ning, Y.F., Hu, C.Y., Xie, S.C., 2016. Antarctic link with East Asian summer monsoon variability during the Heinrich Stadial-Bølling interstadial transition. *Earth and Planetary Science Letters* 453, 243–251.

Zhang, H.W., Cheng, H., Spötl, C., Cai, Y.J., Sinha, A., Tan, L.C., Yi, L., *et al*., 2018. A 200-year annually laminated stalagmite record of precipitation seasonality in southeastern China and its linkages to ENSO and PDO. *Scientific Reports* 8, 12344.

Zhang, J.W., Liu, S.S., Liu, D.B., Kong, X.G., Fang, Y.F., 2019. Correlation of speleothem $\delta^{18}O$ and $\delta^{13}C$ variability from Tian'e Cave, central China: insights into the phase relationship between Asian summer and winter monsoons. *Journal of Asian Earth Sciences*, submitted.

Zhang, T.-T., Li, T.-Y., Cheng, H., Edwards, R.L., Shen, C.-C., Spötl, C., Li, H.-C., Han, L.-Y., Li, J.-Y., Huang, C.-X., Zhao, X., 2017. Stalagmite-inferred centennial variability of the Asian summer monsoon in southwest China between 58 and 79 ka BP. *Quaternary Science Reviews* 160, 1–12.

https://doi.org/10.1017/qua.2019.36 Published online by Cambridge University Press